Original Paper

Eletrônica de Potência
Open Journal of Power Electronics

Received July 05, 2024; accepted October 02, 2024; Date of publication October 16, 2024.
The review of this paper was arranged by Associate Editor Francisco D. Freijedo and Editor-in-Chief Heverton A. Pereira.

Digital Object Identifier http://doi.org/10.18618/REP.e202442

Enhancing SRM Performance through Multi-Platform Optimization and FPGA-Based Real-Time Simulation

Gustavo Xavier Prestes[1,2], **Filipe Pinarello Scalcon**[3], **Babak Nahid-Mobarakeh**[4], **Rodrigo Padilha Vieira**[1]

[1]Federal University of Santa Maria, Power Electronic Engineering Group, Santa Maria, RS, Brazil.
[2]Federal University of Roraima, Department of Electrical Engineering, Boa Vista, RR, Brazil.
[3]Department of Electrical and Software Engineering, University of Calgary, Calgary, AB T2N 1N4, Canada.
[4]McMaster Automotive Resource Center, McMaster University, Hamilton, ON L8P 0A6, Canada.

e-mail: gustavo.prestes@acad.ufsm.br,filipescalcon1@gmail.com, nahidmb@mcmaster.ca, rodrigovie@gmail.com.

ABSTRACT This paper proposes a multi-platform algorithm methodology in order to define firing angles of torque sharing functions (TSFs) for the indirect torque control of switched reluctance motors (SRM) through a hardware-in-the-loop (HIL) system. This proposal is used to achieve optimal levels of torque ripple and losses with accuracy and reliability, while taking advantage of real-time simulation. The analysis is performed assuming steady-state conditions of speed and torque reference for levels below the base speed, aiming to obtain firing angles ensuring optimal tracking performance. A novel methodology is proposed by using a grid search algorithm that handles the communication between Python, Code Composer, and the Typhoon HIL device. For that, an experimental data FPGA-based model with 500 ns of simulation time step is used to ensure highly accurate dynamic responses of current and electromagnetic torque. Moreover, controller-HIL (C-HIL) is used to have a safe and high fidelity testing environment, allowing rapid testing before transitioning to an experimental test bench. The simulation results are experimentally validated, demonstrating that the proposed strategy is effective and ensures optimal performance, taking into account peripheral systems of A/D, signal conditioning, PWM, and sensor emulation.

KEYWORDS Hardware-in-the-loop, multi-platform algorithm, torque sharing function, switched reluctance motor.

I. INTRODUCTION

Swiched Reluctance Motors have been the subject of research in transportation electrification as an alternative solution to permanent magnet synchronous motors (PMSM) and induction motors (IM). It presents several attractive characteristics to the automotive, aviation, and industrial sectors, which include a simple structure, robustness, fault-tolerant capabilities, absence of magnets, and low manufacturing costs [1]–[8]. However, some drawbacks are present such as high non-linearity, torque ripple and acoustic noise [9]. In this context, TSF methods are employed to mitigate torque ripple, sharing torque production between incoming and outgoing phases and providing a suitable current reference for the motor [10]–[14]. On the other hand, this method presents significant offline computational burden while also requiring optimization and accurate models in order to determine the optimal firing angles.

Several methods can be employed to obtain the SRM model by means of offline procedures, such as an experimental data-based model using lookup tables [15], neural networks [16], analytical methods [17], Finite Element Analysis (FEA) or equivalent magnetic circuits [18]. In terms of accuracy, the lookup table based model presents more precise SRM magnetization curves, allowing for a more reliable model to be obtained [15].

As previously mentioned, besides model accuracy, the use of computationally expensive algorithm is required to determine the optimal firing angles for a TSF method. In this regard, the standard offline simulation procedure is highly susceptible to small simulation time step, resulting in an exponential simulation time increase with a linear decrease of time step. Therefore, this method may yield an exceedingly long simulation time, which is undesirable. To avoid such time-consuming procedure, the literature commonly use meta-heuristic algorithms, such as the genetic algorithm (GA), aiming to the optimize conduction angles. In [19] and [20], the authors optimize analytical TSFs using GA, which typically serves as a baseline reference for others TSF type strategies. In [21], the authors proposed a optimization-based TSF with bi-objective GA with higher time-consuming optimization problem. In [22], the authors present a time-efficient torque shaping method based on a linear space approach. This enables a less time-consuming process when compared to bi-objective GA described before, which uses a lookup table based approach, but has high complexity for reproduction. The information presented is summarized in the form of Table 1, showing the GA method as a

TABLE 1. Summary and Comparison of the TSF optimized strategies.

Publication	Optimization algorithm	TSF type	Time-consuming	Implementation complexity	Torque ripple
Proposed	Multi-platform with Grid-search	Analytical	Low	Low	Medium
[19]	Multi-objective GA	Analytical	Medium	Medium	Medium
[20]	Multi-objective GA	Analytical adjusted	Medium	Medium	Medium/Low
[21]	Multi-objective GA	Flux linkage-based	Medium	Medium	Low
[22]	Multi-objective GA	Torque mapping-based	Low	High	Low
[23]	Multi-objective GA	Current dynamic-based	Extremely High	High	Extremely Low
[24]	Multi-objective GA and Golden selection	Current dynamic-based	High	High	Extremely Low

commonly used algorithm, the type of TSF utilized, the time-consuming, the implementation complexity, and the level of torque ripple obtained. In [23] and [24], the authors propose an improved optimization-based TSF with high current tracking performance and reduced torque ripple by a bi-objective optimization approach. However, the time required to perform each step of the optimization is doubled, given that two simulations are required to generate the reference current.

Among the approaches described, it is observed that hardware-in-the-loop (HIL) simulation has not been considered in literature as a means to optimize TSFs. The HIL simulation is a well established technique which features high accuracy models with very short simulation time step and high a fidelity testing environment. This technology received attention in several critical applications involving electric drives [25], [26]. This method has integration between a field programmable gate array (FPGA) - used to build the model, and a digital signal processing (DSP) - used as a device for processing the control algorithm and sending signals to the drive system [27]. This simulation tool has a rapid integration procedure, allowing to reduce the design time by simulating the system at a faster pace, while still exhibiting high accuracy. Furthermore, the use of the DSP allows the user to replicate the same control code that will be used in the experimental setup, which results in greater reliability and fidelity. Then, it is possible to infer that the accuracy of the simulation is more evident when the FPGA model is associated with the intended microprocessor, which takes into consideration A/D measurements, PWM modulation and control algorithms.

A number of papers in the literature discuss the use of machine simulations with HIL devices. In [27], the authors address a review of electrical machines models using HIL simulators. It describes some of the alternatives available in the market in terms of software and hardware, and it presents a PMSM machine model as a case study. In [28], it is described an implementation of an SRM HIL model with lookup tables obtained by FEA. A performance comparison is also performed between the HIL and off-line simulation results. In [29], the authors discuss a HIL system for PMSMs, IMs and SRMs model testing based on FPGA technology using input and output interfaces. In [30], a model based on magnetic equivalent circuits of an SRM is developed by emulating the salients profile and air gap as resistance and voltage sources, aiming for 160 MHz of maximum sampling frequency in a HIL simulation. Similarly, in [18], a novel equivalent magnetic circuit model is proposed, which is validated though experimental results and FEA.

Therefore, the literature shows the interest in SRM systems with high accurate models and small execution time, which ensures reliable design of control systems. These features are aligned with HIL simulation. Although the SRM model HIL approach with a high-fidelity experimental-based model is known, it has not been utilized for TSFs with optimized firing angles, particularly when considering computationally expensive algorithms. Its flexibility and increased performed has not been considered as a means to obtain firing angles in a reduced time. Moreover, the literature has not taken into account, up to this point, the possibility of the optimization process being more effective when using the same test bench microprocessor, considering the firing angles accuracy and better transition process between design and experimental stages.

In this context, this paper presents a strategy for the design and evaluation of TSFs using a HIL approach through a multi-platform algorithm that ensures effective interaction between the devices. The proposed method ensures accurate simulation results through 500 ns time step on an FPGA-based model of a 12/8, 3-phase SRM and asymmetric half-bridge converter (AHB) by using a Typhoon HIL 604 device. The digital microcontroller TMS320F28335 controlCARD is used as the control hardware device. Furthermore, the strategy allows to obtain simulation results in a lower time, by means of continuous real time simulation. The design of analytical TSF with hysteresis current controller (HCC) is implemented with 40 kHz sampling frequency. The performance is evaluated, up to base speed, in steady state operation for different speeds and torque references through a grid search approach. Experimental tests are obtained to compare with the HIL simulation results, demonstrating the effectiveness of the proposed method.

The following topics summarize the main contributions of this paper:

1) The selection of optimal firing angles is achieved using a multi-platform algorithm strategy that employs torque ripple and losses as the cost function.

2) An evaluation of TSFs using a HIL data approach. Enhanced current accuracy data is achieved through the FPGA-based model, integrating the digital microprocessor with A/D peripherals, signal conditioning, PWM, and sensor emulation systems.

3) Data acquisition in real-time mode by using the hardware-in-the-loop device, allowing an optimization-based design approach in less time.

To illustrate the proposed methodology, Figure 1 presents the implementation steps that serve as the basis for defining the sections of this paper.

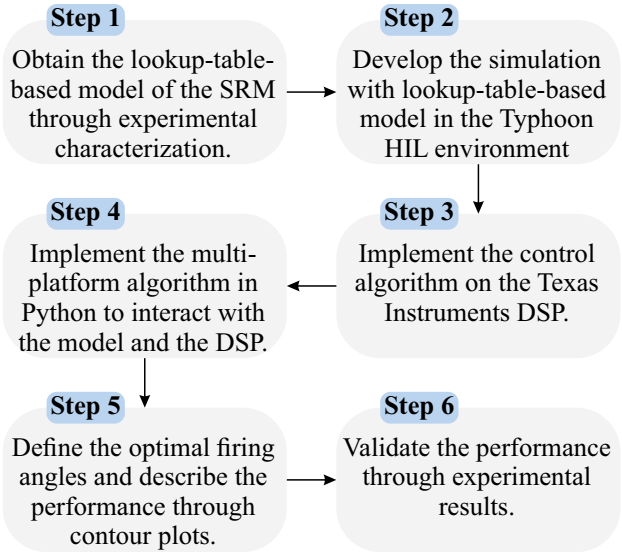

FIGURE 1. Stepwise description.

II. SRM MODEL

This section describes the process of experimental characterizing of the SRM to generate lookup tables that accurately represent the nonlinear behavior of current and electromagnetic torque. Therefore, the block diagram, presented in Fig. 5, depicts the simulation architecture used in the Typhoon HIL environment as FPGA architecture.

A. Experimental SRM Characterization

Continuous torque production is achieved in an SRM by sequentially exciting phases as the rotor poles move towards the stator poles. The machine presents a highly nonlinear behavior for a number of reasons. First, it often operates in a magnetically saturated condition. Moreover, it presents variable inductance that depends on machine's current and phase angular position. Therefore, experimental data based models are typically used in order to achieve more reliable simulation results [15].

The procedure consists of applying a voltage step to one phase of the machine with the rotor locked and, via oscilloscope, storing the voltage and current data for different positions of the machine shaft. In turn, the induced magnetic flux is obtained by calculating the following expression,

$$\phi_{ph} = \int_0^t (v_{ph} - Ri_{ph})\, dt \tag{1}$$

where, ϕ_{ph} is the flux linkage, v_{ph} is the voltage, R is the winding resistance, and i_{ph} is the current of each phase.

The flux linkage profile for the studied 12/8 SRM are given in Figure 2(a). This result is obtained through spline interpolation in order to build a linearly spaced lookup table. It should be noted that the interpolation technique allows the experimental data to be extended to unsampled rotor position intervals. The detailed procedure for machine characterization can be observed in the paper [15]. The rated parameters of the SRM are presented in Table I.

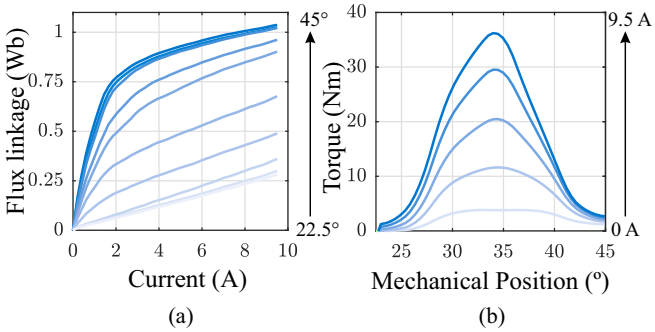

FIGURE 2. SRM data. (a) Flux linkage profiles and (b) Electromagnetic torque profile.

TABLE 2. 12/8 SRM parameters.

Parameter:	Value
Rated speed	1500 r/min
Rated power	2 kW
Rated toque	12.73 Nm
Rated voltage	400 V
Rated RMS current	5 A
Number of phases	3

Similarity, the electromagnetic torque profile, shown in Fig. 2(b), can be obtained initially by calculating the co-energy. It is defined as the integral of flux linkage in relation to current. Therefore, the co-energy can be described as

$$W_{ph}^{co} = \int_0^i \phi(\theta, i) di. \tag{2}$$

where, W_{ph}^{co} is the co-energy considering to each machine phase.

Thus, the total co-energy is the sum of the co-energy of each phase as described in

$$W^{co} = \sum_{ph=1}^{3} W_{ph}^{co}(i,\theta). \tag{3}$$

Finally, the electromagnetic torque can be determined as the partial derivative of the co-energy with regards to the angular position, defined as

$$T_e = \frac{\partial W^{co}}{\partial \theta}. \tag{4}$$

Based on the curves obtained in Fig. 2 it is possible to build up two lookup tables. Current lookup table, $i(\phi,\theta)$, which outputs the current value based on the flux linkage and rotor position, and a torque lookup table, $T_e(i,\theta)$, which outputs the torque value based on the current and rotor position. The surface results of $i(\phi,\theta)$ and $T_e(i,\theta)$ are presented in the Fig. 3 and 4 respectively, illustrate the interval related to the generator and motor operation cycle.

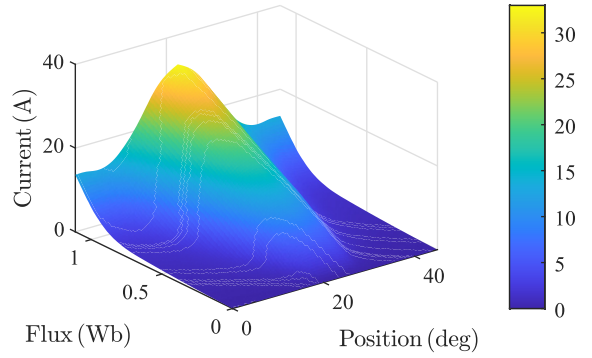

FIGURE 3. Surface of $i(\phi,T)$.

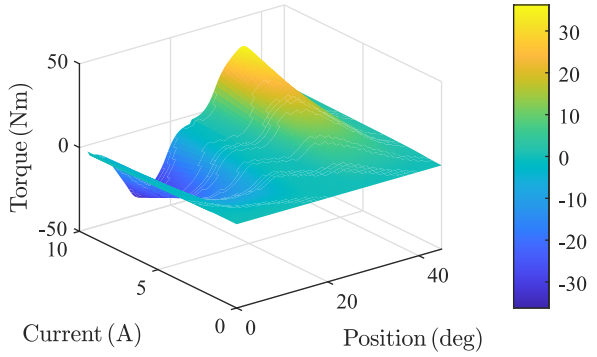

FIGURE 4. Surface of $T(\theta,i)$.

These tables are essential for SRM simulation, which will be used in the FPGA-based simulation through a Typhoon HIL environment. The detailed description of the simulation procedure is presented next.

B. Lookup-table-based Simulation

The dynamic behavior of the SRM can be emulated through lookup-table based on (1), and $i(\phi,\theta)$ and $T_e(i,\theta)$, as depicted in the block diagram shown in Figure 5.

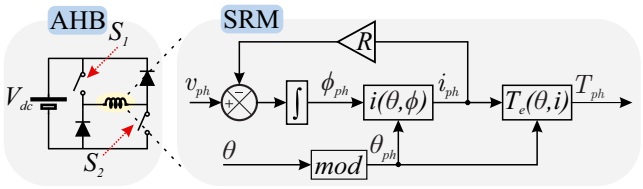

FIGURE 5. Lookup-table-based model simulation of SRM.

The $i(\theta,\phi)$ and $T_e(\theta,i)$ tables are stored in the Typhoon HIL simulation environment. The phase voltage v_{ph} is supplied through an AHB converter, and the angular position is emulated using digital signals that replicate a quadrature encoder. A simulation integration step of 500 ns is employed to ensure high fidelity in capturing the machine's dynamic current behavior.

S_1 and S_2 are upper and lower switches for each phase. These are controlled through the microcontroller according to computed indirect torque control algorithm that is described in the following section.

III. CONTROL ALGORITHM

This section presents the control law used for the algorithm's implementation on the microcontroller. First, the TSF is detailed as a method for converting the reference torque into a phase-specific reference current. Following this, the HCC, associated with the chopping regions method, is introduced.

Figure 6 presents the block diagram representing the structure of the indirect torque control system.

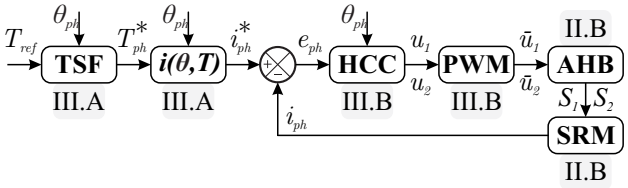

FIGURE 6. Block diagram of indirect torque control.

where T_{ref} is an equivalent reference torque, T_{ph}^* is the instantaneous torque reference based on the phase angular position θ_{ph}, generated by the TSF, e_{ph} is the error between the phase current reference (i_{ph}^*) resulting from the torque-current conversion and the measured phase current (i_{ph}). u_1 and u_2 are the HCC signals corresponding to the upper and lower switches, respectively. These signals are conditioned by PWM modulation, generating the signals $\bar{u}_1$ and $\bar{u}_2$ for the converter that drives the SRM through the switching of S_1 e S_2.

The AHB and SRM blocks were previously discussed in Section II.B. From this point forward, the TSF and $i(\theta,T)$ are presented in Section III.A, and the HCC and PWM blocks are described in Section III.B.

A. Torque Sharing Function

Especially used for torque ripple mitigation, TSFs are a form of indirect torque control of switched reluctance motors. The

TSF distributes the equivalent torque among different phases by generating a dynamic reference current according to the mathematical model of the machine.

The algebraic TSFs have overlapping intervals usually described by linear, sinusoidal, cubic, and exponential functions [19]. This work will be limited to presenting the sinusoidal function as an example of the approach. The mentioned function is shown in Fig. 7 as described by [20]. Additionally, it presents the angles for forming the desired phase torque profile.

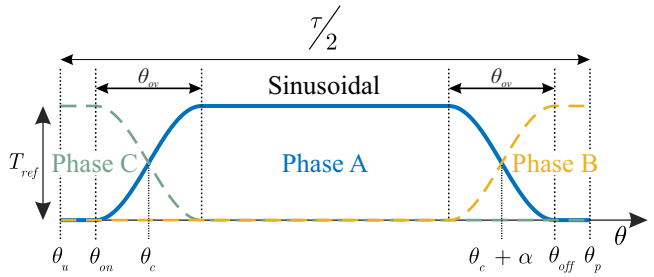

FIGURE 7. Sinusoidal TSF profile.

By adopting the 12/8 SRM as the object of study and considering that the machine's drive cycle is described by $\tau = 360°/N_r$ (where N_r is the number of rotor poles), there is an interval of $45°$ that encompasses both generator and motor operation cycles. However, this work's proposal is limited to the motor operation approach, therefore only half of the operation cycle is used. The starting angle is $\theta_u = 22.5°$ and the final angle is $\theta_p = 45°$.

The main angles that define the phase torque profile are θ_{on}, which initiates the magnetization phase, θ_{ov}, which defines the overlap interval, and θ_{off}, which marks the end of the demagnetization period, expressed as:

$$\theta_{off} = \theta_{on} + \theta_{ov} + \alpha \tag{5}$$

where $\alpha = 360°/(mN_r)$ is the displacement between adjacent phases. Given that m is the number of phases and N_r is the number of poles, $\alpha = 15°$. Furthermore, the maximum excursion of θ_{ov} can be defined from the perspective where $\theta_{\text{on}} = \theta_u$ and $\theta_{\text{off}} = \theta_p$. Substituting into (5) yields $\theta_{\text{ov}} = 7.5°$.

Between the output and input phases, θ_c determines the central point of torque balance between the phases and can be expressed as a function of θ_{on}, θ_{ov}, and θ_{off}, as follows:

$$\theta_c = \theta_{on} + \frac{\theta_{ov}}{2} = \theta_{off} - \frac{\theta_{ov}}{2} - \alpha \tag{6}$$

Regardless of the profile of interest, the instantaneous torque is obtained through the sequencing of steps conditioned by the intervals that depend on the angles θ_{on}, θ_{ov}, and θ_{off}. Therefore, the TSF can be systematized by:

$$T^*_{ph} = \begin{cases} 0, & 0 \le \theta_{ph} \le \theta_{on} \\ T_{\text{ref}} f_{\text{rise}}(\theta_{ph}), & \theta_{on} < \theta_{ph} < \theta_{on} + \theta_{ov} \\ T_{\text{ref}}, & \theta_{on} + \theta_{ov} \le \theta_{ph} \le \theta_{off} - \theta_{ov} \\ T_{\text{ref}} f_{\text{fall}}(\theta_{ph}), & \theta_{off} - \theta_{ov} < \theta_{ph} < \theta_{off} \\ 0, & \theta_{off} \le \theta_{ph} \le \theta_p, \end{cases} \tag{7}$$

The functions $f_{rise}(\theta_{ph})$ and $f_{fall}(\theta_{ph})$ are used to generate a reference torque profile between two adjacent phases, whose sum results in the desired equivalent torque. The function $f_{rise}(\theta_{ph})$ increases from 0 to 1 when θ_{ph} is between the initial magnetization reference, θ_{on}, and the final interval of the rise function, as defined by $\theta_{on} + \theta_{ov}$.

The $f_{rise}(\theta)$ function is defined by:

$$f_{rise}(\theta_{ph}) = \frac{1}{2} - \frac{1}{2}\cos\left(\pi \frac{(\theta_{ph} - \theta_{\text{on}})}{\theta_{\text{ov}}}\right) \tag{8}$$

If θ_{ph} is between the final magnetization interval and the beginning of the demagnetization interval defined by $\theta_{off} - \theta_{ov}$, $T^*_{ph} = T_{ref}$. If θ_{ph} is greater than $\theta_{off} - \theta_{ov}$, $f_{fall}(\theta_{ph})$ decreases from 1 to 0 until the final demagnetization interval defined by θ_p. Regardless of the type of TSF, the function $f_{fall}(\theta_{ph})$ can be represented by:

$$f_{fall}(\theta_{ph}) = 1 - f_{rise}(\theta_{ph} + \theta_{on} + \theta_{ov} - \theta_{off}) \tag{9}$$

To obtain the current reference, is necessary to interpolate the function $i(\theta, T)$. This function can be derived through the inversion procedure of the original $T(\theta, i)$ lookup table presented in Fig. 4. This procedure is described by [1], and the result is presented in Fig. 8.

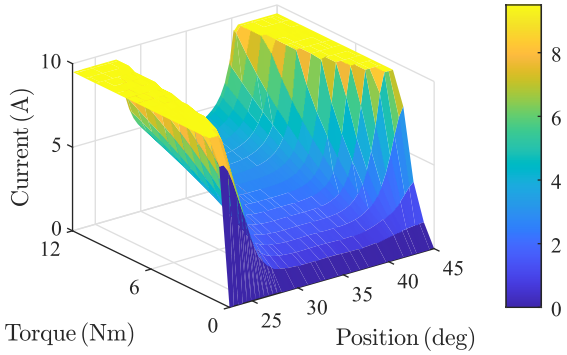

FIGURE 8. Surface of $i(\theta, T)$.

B. Hysteresis Current Controller

The reference current generated by the TSF is tracked by a HCC, as described in the block diagram shown in Fig. 6. This method is simple and robust, but it has drawbacks, such as the need for high sampling rates and variable switching frequency. To address these issues, a 40 kHz sampling rate was adopted for the controller, in line with the maximum performance capability of the microcontroller. Additionally,

the chopping region method was implemented to reduce current tracking variation, particularly in regions of lower inductance.

Fig. 9 highlights the operational stages of the AHB converter with respect to soft chopping (SC) and hard chopping (HC), as shown in Fig. 9(a), and their association with torque and current reference, as illustrated in the example shown in Fig. 9(b).

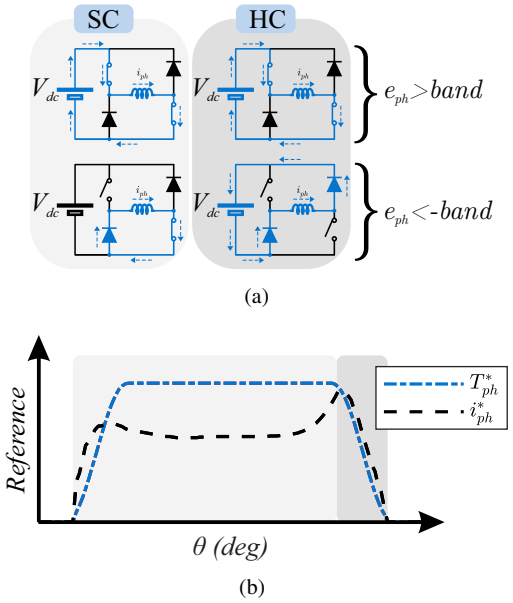

FIGURE 9. Soft chopping and hard chopping control mode. (a) AHB with chopping operational stages. (b) Example of torque and current reference with chopping region highlight.

The first stage is the magnetization of the winding, which occurs when $e_{ph} >$ band, and is common to both SC and HC modes, at which point the voltage V_{dc} is applied to the phase. When $e_{ph} < -$band, SC and HC operate differently. For SC, zero voltage is applied to the phase, operating in freewheeling mode, where the current flows only through the phase, a switch, and a diode. For HC, it operates in demagnetization mode, as $-V_{dc}$ is applied to the phase when both switches are turned off, allowing the current to flow through the phase and both diodes.

As described, the HCC presented in this section is implemented in the microcontroller, as well as the algorithm for obtaining the reference current, the TSF, and the function $i(\theta, T)$ presented before, which are implemented using bilinear interpolation.

The control signals generated by the HCC are calculated at a fixed frequency and normalized between 0 and 1 according to the PWM carrier signal. The resulting comparison of the signals is used to turn on and turn off the switches.

With the implementation of the control algorithm completed, the next section discusses the optimization process used to determine the firing angles. It will present the cost function used and the proposed multi-platform algorithm.

IV. OPTIMIZATION-BASED PROBLEM

TSFs provide a low torque ripple and often enable a secondary objective to be considered. However, the firing angles design present a non-trivial selection process. Depending on firing angles chosen, the results of torque ripple and current profile will differ for the same operating point. Usually, an approach used to resolve this trade-off is to address the problem by defining a cost function that takes the desired performance parameters into account.

In the discrete-time approach, the RMS current can be represented by:

$$I_{RMS} = \sqrt{\frac{1}{N}\sum_{k=1}^{N} i_{ph(k)}^2} \tag{10}$$

where N is the total number of points within a sampling interval, k is the index of the data vector, and i_{ph} refers to each of the sampled phases.

Furthermore, the cost function must also represent the torque ripple, which is defined by:

$$T_r = \frac{\max(T_e) - \min(T_e)}{\text{mean}(T_e)} \tag{11}$$

where T_e is the equivalent electromagnetic torque obtained by summing the instantaneous torque resulting from each phase.

Finally, the minimization of the performance parameters can be implemented by solving the optimization problem described by:

$$\min_{\theta_{\text{on}},\theta_{\text{ov}}} J = ||I_{RMS}|| + ||T_r||$$
$$\text{subject to} \begin{cases} \theta_{\text{off}} - \theta_{ov} - \theta_{ov} - \alpha = 0, \\ \max(i^*_{ph}) - I_{\max} \leq 0, \\ \theta_{\text{ov}} - 2(\theta_c - \theta_u) \leq 0, \\ \theta_{\text{ov}} - 2(\theta_p - \theta_c - \alpha) \leq 0, \end{cases} \tag{12}$$

where $||I_{RMS}||$ and $||T_r||$ are the normalized RMS current and torque ripple respect to maximum values found for each torque-speed operation condition, in order to compatibilize the performance parameters of different quantities.

The constraints for the problem define the necessary conditions for potential candidates for the current profile. It is assumed that the potential candidates must be within the phase conduction cycle, result in unsaturated current profiles, and meet the overlapping limits in the magnetization and demagnetization segments. Furthermore, the torque-sharing current reference must be properly tracked. Authors such as [1], [20] describe that this reference should not be faster than the machine dynamics. Considering that, this paper takes into account the rate of current change according to the limits of the bus voltage and operating speed.

From this point forward, the next step is to implement the algorithm that will test each possible combination of θ_{on}

and θ_{ov} and capture the current and torque data generated in the simulation in order to calculate the cost function (12).

For this reason, the following section presents a methodology to find optimal firing angles aiming to minimize torque ripple and RMS current through multi-platform algorithm strategy. This approach ensures high accuracy and reliability with rapid simulation process, characteristics inherent to the real-time simulation.

V. MULTI-PLATFORM ALGORITHM STRATEGY

This section describes the multi-platform algorithm strategy, which aims to determine the firing angles through an optimization procedure that relies on iterative communication between different platforms and simulation and control devices. Fig. 10 illustrates the steps used in the development of the algorithm.

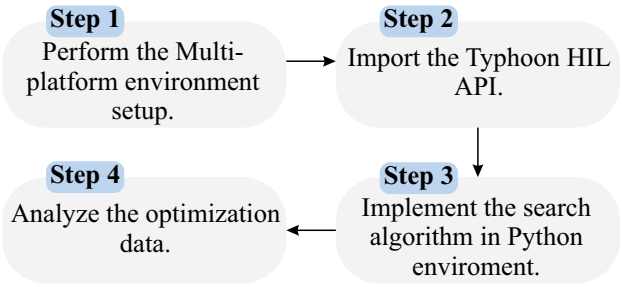

FIGURE 10. Steps taken for the development of the multi-platform algorithm.

The first step involves a pre-development stage, serving as the framework for proper communication between environments and devices. In this stage, the systems must be configured according to the version in which the model was developed within the Typhoon HIL environment. For this work, Typhoon HIL Control Center V2023.2 was used, along with Python Programming Language 3.11.5 and Typhoon-HIL-API 1.23.1, through a multi-platform algorithm that interfaces between the devices.

The second step involves importing the Typhoon-API. This tool is responsible for ensuring communication between the Python algorithm and the HIL device. It allows for the transmission of digital signals through the general purpose input/output (GPIOs), which are provided by the interface board between the microcontroller and the hardware-in-the-loop simulation device.

The third step is the development of the proposed algorithm, which will be described in detail through the pseudocode shown in Fig. 12.

The fourth step is related to the analysis of the obtained data. The optimal firing angles, as well as the performance parameters, are stored and analyzed.

To accomplish this, HIL simulation is performed using Typhoon HIL hardware which is composed of a real time HIL 604 device and a DSP interface 3.0. In addition, the setup also contains a Texas Instrument TMDSCNCD28335 DSP control card, and a host computer with an Intel i7-6500U CPU, and 8GB of RAM. The components of the HIL setup are presented in detail in Fig 11.

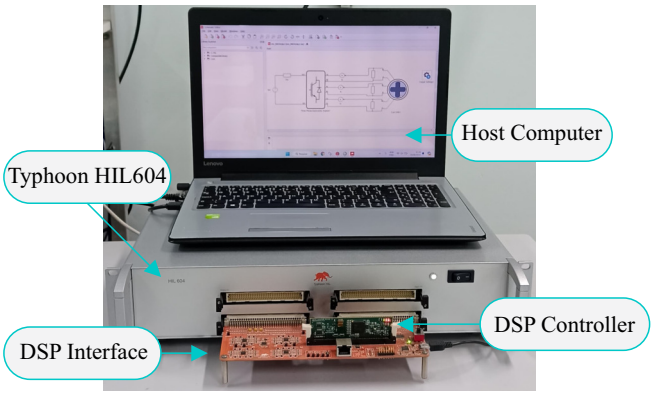

FIGURE 11. HIL simulation setup.

This algorithm is presented by means of a schematic description in Fig. 12 through three-layer illustration.

Layer 1: Python code, as pseudo code described, is deployed on the personal computer and include the base algorithm that computes the cost function and all calculations necessary to implement the firing angles selection procedure steps. In this layer, a linear grid of firing angles is created and then updated according to constraints in (12). In order to reduce computing effort only two values of reference torque are used, 1 Nm for minimum and the maximum torque traceable according to the rotor speed and the implemented TSF. Typhoon HIL Application Program Interface (*typhoon.api*) is used to load the SRM lookup table model developed in the FPGA-based environment. Furthermore, the analog to digital converters are defined to measure the currents and equivalent torque behavior. A continuous simulation is performed for each rotor speed, torque reference and possible firing angles. The torque and firing angles are quantized, transforming the values to digital, which are then sent to the DSP through GPIOs. After an electrical cycle, the currents and torque are sampled in order to compute the defined cost function. Finally, the performance parameters are stored and the simulation is stopped.

Layer 2: Microcontroller algorithm is where the TSF and current control algorithm are implemented. In this regard, an HCC algorithm with hybrid chopping region control (as described in [9]) is chosen due to its simplicity and the fact it is often used for this system. The binary data is received through GPIOs and converted up to sinal according to digital to analog converter and dequantized process. Then, the interruption of the control algorithm in 40 kHz is performed defining the phase torque reference, T^*_{abc}, produced by the TSF block which has inputs such as T_{ref}, and the phase current value is obtained through bilinear interpolation of $i(\theta, T)$. Besides, integrated peripherals such as eQEP and ePWM are used to measure rotor position and generate PWM signals based on the outputs of the HCC, respectively.

Layer 1 - Python code

1: **Start.**
2: Create a firing angle vectors regularly spaced:
θ_{on} = 23°:0.1°:28°
θ_{ov} = 1°:0.1°:7.5°
3: Update firing angles according to constraints described in (12) and rate of flux.
4: Find the maximum torque operation for each speed.
5: Define points operation: ω_r and T_{ref}.
6: Load HIL model through API Typhoon HIL.
7: Define the ADCs for currents and torque measurements.
8: Run simulation.
9: **for** each ω_r **do**
10: **for** each T_{ref} **do**
11: **for** each combination of firing angles update **do**
12: Perform data quantization.
13: Send the data to the DSP through the GPIOs.
14: Sample i_a, i_b, i_c and T_e in each electric cycle.
15: Compute (10-12).
16: **end**
17: **end**
18: **end**
19: Store data.
20: Stop Simulation.
21: **End.**

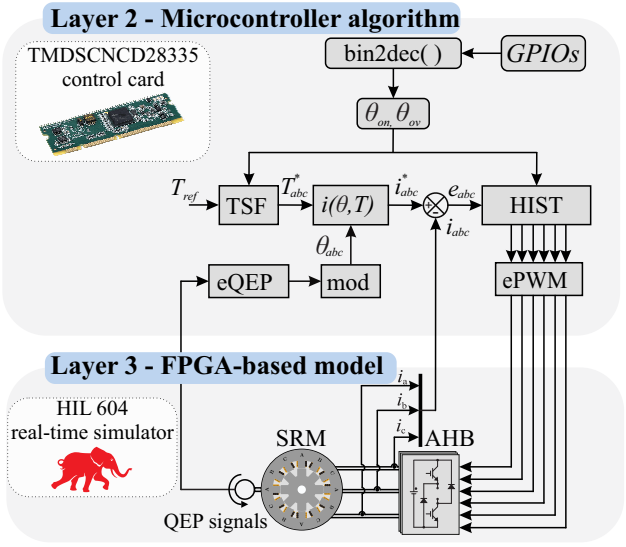

FIGURE 12. Flowchart of the firing angle optimize procedure.

Layer 3: FPGA-based model is the model that is implemented in the Typhoon HIL schematic editor software with 500 ns time step in simulation real-time mode. It receives the PWM signals from the microcontroller and drives the switches of the AHB three-phase inverter. The phase currents are measured through the analog outputs provided by the device and the angular position is then sent through digital QEP signals to the microcontroller, emulating the behavior of an incremental encoder.

After completing the optimization step using the multi-platform algorithm, the firing angles are evaluated in the following section for the specified torque-speed operating points. In this process, the optimal angles are determined and then tested experimentally in Section VII to validate the proposed approach.

VI. EVALUATION OF SELECTED FIRING ANGLES

This section presents a case study of the optimization procedure outlined in the previous section. The firing angles are determined based on rotor speeds ranging from 100 rpm to 1000 rpm, which represent the range for operations below the base speed, where current control can be achieved due to DC link is grater than back-EMF. Furthermore, a minimum reference torque of 1 Nm and a maximum reference torque that varies according to speed. Linear regression is utilized to define the firing angles for untested intervals.

In order to illustrate an optimal solution, Fig. 13 shows a contour plot that represents the cost function in relation to the firing angles. It is possible to observe that the set of solutions exhibits varying levels, even including local minima. Nevertheless, the grid search ensures the global minimum within the adopted precision margin of 0.1° is found, represented by red point.

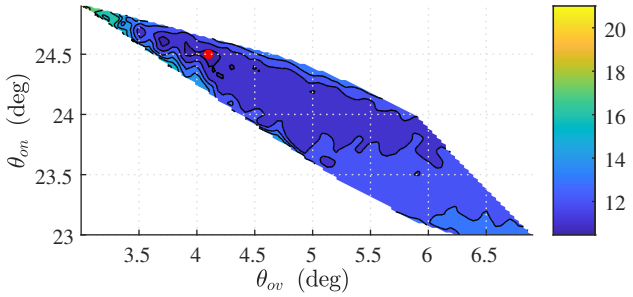

FIGURE 13. Cost function regarding for 200 rpm at a 12 Nm load.

A. Contour Map Analysis

Through the set of simulations performed for each operating point, it is possible to obtain the cost function values for the entire search space for the function described in (12). These values are represented as a function of θ_{on} and θ_{ov}. Therefore, the performance of the parameters can be verified with respect to torque-speed evaluation, as illustrated in Fig. 14, which shows the operating conditions for the sinusoidal TSF. Next, the performance at low, medium, and high-speed operating points is presented through hardware-in-the-loop simulation. Fig. 14 (a) and (b) correspond to firing angles defined according to the HIL results and evaluation criteria described previously. It is noted that as speed increases, there is a region of low torque and low speed where the activation angle is larger, and as torque or speed increases, this measure tends to decrease. This characteristic occurs complementarily for the overlap angle, which shows lower values for lower speeds and torque, but increases in response to these references.

The performance parameters used in the cost function, torque ripple and RMS current, can be observed in Fig. 14 (c)

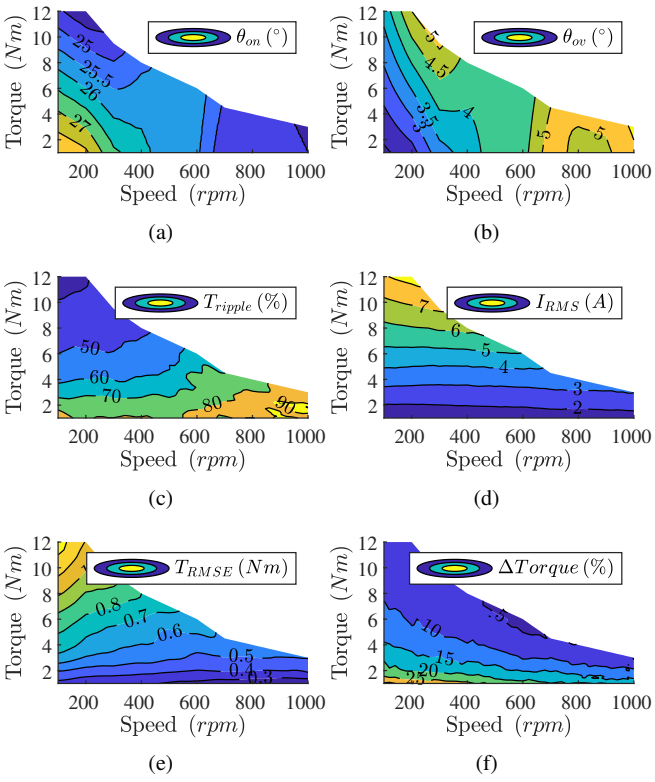

FIGURE 14. Torque-speed reference contour behavior. (a) turn-on angle, (b) overlap angle, (c) torque ripple, (d) RMS current, (e) RMSE torque and (f) relative rate of change of torque with respect to reference.

and (d), respectively. Considering a balance factor between the metrics, it is possible to observe lower levels of torque ripple at low-speed and high-torque operating points. As the speed increases, higher levels are observed, reaching up to 90%. The current levels, in turn, are primarily determined by the operating torque, with little influence from changes in speed.

The Root Means Square Error (RMSE) and relative rate of change of torque can be observed in the Fig. 14 (e) and (f). The first presents the effective tracking error, that can be obtained through $(\sum_{k=1}^{N}(T_e(k)-T_{ref}(k))^2)^{1/2}$, showing higher values with increasing torque. However, the $\Delta(\%)$ indicates the error relative to the reference torque, highlighting that the current controller performs worse at low torque levels, and can be obtained through $(T_{rms}/T_{ref}-1)\times 100$.

B. Steady-state HIL Simulation

As a means to evaluate the performance of current tracking and the resulting torque according to the selected firing angles, steady-state tests are conducted. Fig. 15 presents the HIL simulation results of the controller under 12 Nm at a speed of 200 rpm. At this operating point, the torque ripple is minimal for the proposed system and demonstrates the effectiveness of the firing angles selection stage in compensating for the torque ripple resulting from the phase commutation.

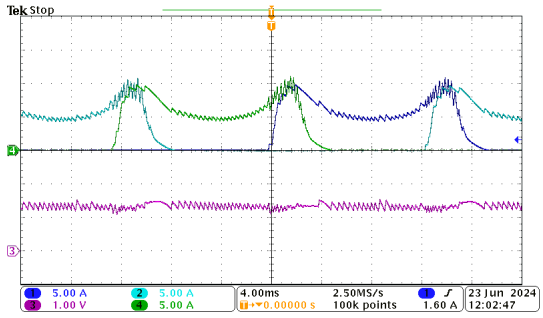

FIGURE 15. HIL results for speed of 200 rpm and a 12 Nm load. Channels 1, 2 and 4 represent the phase currents with a scale of 5A/div. Channel 3 represents the electromagnetic torque with a scale of 10 Nm/div.

With $\theta_{\text{on}} = 24.1°$ and $\theta_{\text{ov}} = 5°$ it can be observed that the RMS torque reaches 13.34 Nm, exceeding the required reference of 12 Nm. This characteristic results from the HCC, where tracking quality is associated with narrower bandwidths and high sampling rates. Despite this characteristic, it was possible to achieve 34.24% torque ripple. Furthermore, 9.09 A RMS was achieved.

With $\theta_{\text{on}} = 25.8°$ and $\theta_{\text{ov}} = 4.1°$, Fig. 16 shows the HIL simulation results of the controller under 6 Nm at a speed of 600 rpm, illustrating the performance at medium speed. The RMS torque was 6.48 Nm with a torque ripple of 62.27% and 5.65 A RMS. The decline in performance was already anticipated by the torque-speed performance analysis. Furthermore, the current output interval shows a higher level due to the advancement of the turn-on angle.

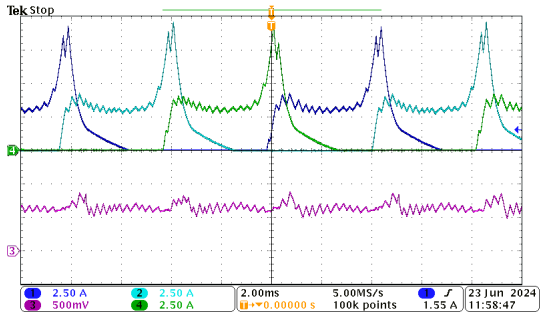

FIGURE 16. HIL results for speed of 600 rpm and a 6 Nm load. Channels 1, 2 and 4 represent the phase currents with a scale of 2.5A/div. Channel 3 represents the electromagnetic torque with a scale of 5Nm/div.

With $\theta_{\text{on}} = 24.3°$ and $\theta_{\text{ov}} = 5.6°$, Fig. 17 shows the HIL simulation results of the controller under 3 Nm at a speed of 1000 rpm. Once more, the torque ripple increases to levels of 74.94% with an RMS torque of 3.25 Nm and 3.31 A RMS. Moreover, the tail current characteristic can be observed more clearly in the untrackable intervals.

Despite the increase in torque oscillation with increasing speed, an inherent characteristic of the analytical TSF, the proposed method demonstrated effectiveness in finding the best solution with rapid simulation capability and reliability.

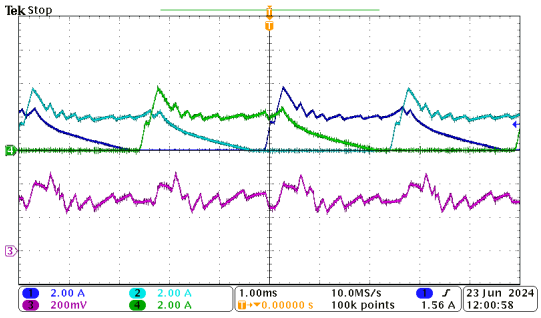

FIGURE 17. HIL results for speed of 1000 rpm and a 3 Nm load. Channels 1, 2 and 4 represent the phase currents with a scale of 2A/div. Channel 3 represents the electromagnetic torque with a scale of 2Nm/div.

The next section presents the experimental results in order to validate the proposed methodology.

VII. EXPERIMENTAL EVALUATION

This section presents experimental results to evaluate the effectiveness of the proposed method, comparing them to the results from the HIL simulation. The SRM used is presented in the Fig. 2 and the machine parameters are given in Table 2. Moreover, the test bench used is shown in Fig. 18, encompassing a TMS320F28335 Texas Instruments DSP. The setup is composed of an SRM coupled to an IM, used as a load. Additional components such as an encoder, three-phase AHB converter, IM inverter, DC supply and a host computer are also used.

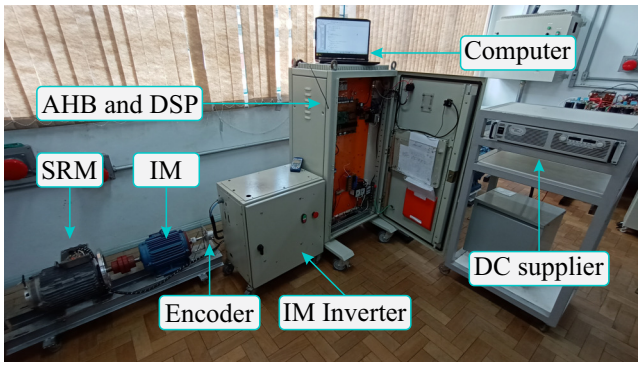

FIGURE 18. Experimental test bench including the SRM, IM, encoder, drives, DC supply and host computer.

The SRM and IM machines have their shafts mechanically coupled and are connected to the same DC supply in regenerative mode. The speed of the IM is controlled by its own three-phase inverter, while the SRM operates in torque control mode as described in Section III, using the optimal firing angles obtained through the proposed algorithm presented in Section V.

The experimental results obtained are described similarly to those presented in the HIL simulation described in the Section VI.B. The measured currents were captured using isolated probes, and the estimated electromagnetic torque was derived through bilinear interpolation $T(\theta, i)$ and generated via DAC conversion with 10, 5 and 3 Nm/div for each phase.

Fig. 19 shows the results for 200 rpm with a reference torque of 12 Nm. It can be observed that the method performs minimization satisfactorily, similar to the results obtained via HIL with 30.25% torque ripple, 12.62 Nm of RMS torque and 7.8 A RMS. However, it is also noticeable that the experimentally obtained currents exhibit a lower switching frequency compared to the model. Note, though, that this is reasonable due to electric parametric uncertainty and non-modeled dynamic effects. Nevertheless, this characteristic does not compromise the design of the firing angles, which are related to the phase commutation interval and remain consistent with the expected minimum and maximum levels. Therefore, the RMS results and torque ripple remained close to the expected values.

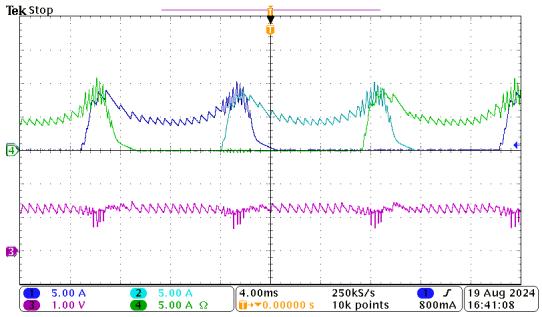

FIGURE 19. Experimental results for speed of 200 rpm and a 12 Nm load for $\theta_{on} = 24.1^\circ$ and $\theta_{ov} = 5^\circ$. The phase currents correspond to channels 1, 2, and 4.

Fig. 20 shows the experimental results of the controller under a 6 Nm load at a speed of 600 rpm. A strong similarity in current performance can be observed, with a slight reduction in peak amplitude during the final demagnetization phase. And, 42.54% torque ripple, 6.05 Nm RMS torque and 4.91 A RMS are obtained.

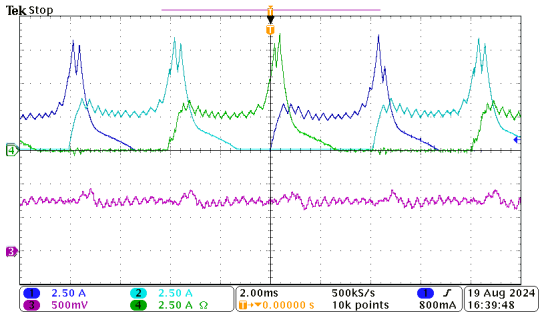

FIGURE 20. Experimental results for speed of 600 rpm and a 6 Nm load for $\theta_{on} = 25.8^\circ$ and $\theta_{ov} = 4.1^\circ$. The phase currents correspond to channels 1, 2, and 4.

Fig. 21 shows the experimental results of the controller under a 3 Nm load at a speed of 1000 rpm. A small reduction in the current level compared to the simulation can be observed, along with a more pronounced nonlinear profile in

the tail current. As a result, a lower level of electromagnetic torque is observed. Lastly, 48.14% torque ripple, 2.89 Nm RMS torque and 2.81 A RMS are observed.

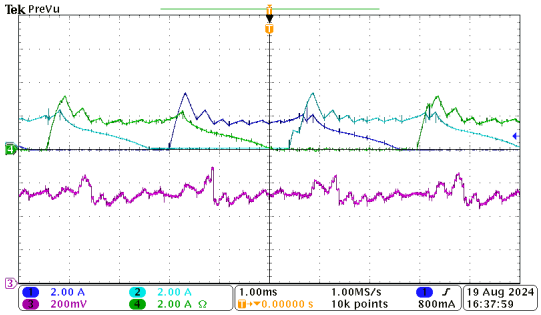

FIGURE 21. Experimental results for speed of 1000 rpm and a 3 Nm load for $\theta_{on} = 24.3°$ and $\theta_{ov} = 5.6°$. The phase currents correspond to channels 1, 2, and 4.

VIII. CONCLUSION

In this paper, a multi-platform algorithm strategy with HIL approach in order to design and evaluation TSF is proposed. An FPGA-based model is used with a digital signal processor to obtain better current and torque accuracy, while enabling fast simulation condition with 500 ns time step in real-time. Furthermore, the methodology allows the designer to quickly transition between simulation and experiment with high fidelity and lower likelihood of implementation errors in the project. This approach provides an early insight into the algorithm and the computational burden of the micro-controller. The contour map analysis provided results that shows performance parameters along torque-speed reference. Nevertheless, the firing angles selection method seeking to simplify and desired performance. The steady-state results in HIL simulation are experimentally validated and shows the effectiveness the method.

ACKNOWLEDGMENT

This study was financed in part by the Coordenação de Aperfeiçoamento de Pessoal de Nível Superior – Brasil (CAPES/PROEX) – Finance Code 001.

AUTHOR'S CONTRIBUTIONS

PRESTES, G.X.: Conceptualization, Data Curation, Formal Analysis, Investigation, Methodology, Software, Validation, Visualization, Writing – Original Draft, Writing – Review & Editing. **SCALCON, F.P.**: Data Curation, Formal Analysis, Validation, Visualization, Writing – Original Draft, Writing – Review & Editing. **NAHID-MOBARAKEH, B.:** Resources, Supervision, Visualization. **VIEIRA, R.P.**: Resources, Supervision, Visualization.

PLAGIARISM POLICY

This article was submitted to the similarity system provided by Crossref and powered by iThenticate – Similarity Check.

REFERENCES

[1] B. Bilgin, J. W. Jiang, A. Emadi, *Switched reluctance motor drives: fundamentals to applications*, CRC press, 2019, doi:10.1201/9780203729991.

[2] G. Fang, F. P. Scalcon, D. Xiao, R. P. Vieira, H. A. Gründling, A. Emadi, "Advanced Control of Switched Reluctance Motors (SRMs): A Review on Current Regulation, Torque Control and Vibration Suppression", *IEEE Open Journal of the Industrial Electronics Society*, vol. 2, pp. 280–301, 2021, doi:10.1109/OJIES.2021.3076807.

[3] D. G. Barroso, Y. Yang, F. A. Machado, A. Emadi, "Electrified Automotive Propulsion Systems: State-of-the-Art Review", *IEEE Transactions on Transportation Electrification*, vol. 8, no. 2, pp. 2898–2914, 2022, doi:10.1109/TTE.2021.3131917.

[4] Z. Q. Zhu, D. Howe, "Electrical Machines and Drives for Electric, Hybrid, and Fuel Cell Vehicles", *Proceedings of the IEEE*, vol. 95, no. 4, pp. 746–765, 2007, doi:10.1109/JPROC.2006.892482.

[5] Z. Yang, F. Shang, I. P. Brown, M. Krishnamurthy, "Comparative Study of Interior Permanent Magnet, Induction, and Switched Reluctance Motor Drives for EV and HEV Applications", *IEEE Transactions on Transportation Electrification*, vol. 1, no. 3, pp. 245–254, 2015, doi:10.1109/TTE.2015.2470092.

[6] S. Dhale, B. Nahid-Mobarakeh, A. Emadi, "A Review of Fixed Switching Frequency Current Control Techniques for Switched Reluctance Machines", *IEEE Access*, vol. 9, pp. 39375–39391, 2021, doi:10.1109/ACCESS.2021.3064660.

[7] E. Bostanci, M. Moallem, A. Parsapour, B. Fahimi, "Opportunities and Challenges of Switched Reluctance Motor Drives for Electric Propulsion: A Comparative Study", *IEEE Transactions on Transportation Electrification*, vol. 3, no. 1, pp. 58–75, 2017, doi:10.1109/TTE.2017.2649883.

[8] G. Fang, J. Ye, D. Xiao, Z. Xia, X. Wang, X. Guo, A. Emadi, "An Intersection-Method-Based Current Controller for Switched Reluctance Machines With Robust Tracking Performance", *IEEE Transactions on Transportation Electrification*, vol. 7, no. 4, pp. 2822–2834, 2021, doi:10.1109/TTE.2021.3086012.

[9] F. P. Scalcon, G. Fang, R. P. Vieira, H. A. Gründling, A. Emadi, "Discrete-Time Super-Twisting Sliding Mode Current Controller With Fixed Switching Frequency for Switched Reluctance Motors", *IEEE Transactions on Power Electronics*, vol. 37, no. 3, pp. 3321–3333, 2022, doi:10.1109/TPEL.2021.3116096.

[10] H. Gao, F. R. Salmasi, M. Ehsani, "Inductance model-based sensorless control of the switched reluctance motor drive at low speed", *IEEE Transactions on power electronics*, vol. 19, no. 6, pp. 1568–1573, 2004, doi:10.1109/TPEL.2004.836632.

[11] J. Ye, B. Bilgin, A. Emadi, "An offline torque sharing function for torque ripple reduction in switched reluctance motor drives", *IEEE Transactions on energy conversion*, vol. 30, no. 2, pp. 726–735, 2015, doi:10.1109/TEC.2014.2383991.

[12] H. Li, *Torque Ripple Minimization in Switched Reluctance Machines*, Ph.D. thesis, 2017.

[13] M. Hamouda, A. A. Menaem, H. Rezk, M. N. Ibrahim, L. Számel, "An improved indirect instantaneous torque control strategy of switched reluctance motor drives for light electric vehicles", *Energy Reports*, vol. 6, pp. 709–715, 2020, doi:10.1016/j.egyr.2020.11.142.

[14] G. Fang, J. Ye, D. Xiao, Z. Xia, A. Emadi, "Computational-efficient model predictive torque control for switched reluctance machines with linear-model-based equivalent transformations", *IEEE Transactions on Industrial Electronics*, 2021, doi:10.1109/TIE.2021.3091918.

[15] T. A. D. S. Barros, P. J. D. S. Neto, M. V. De Paula, A. B. Moreira, P. S. Nascimento Filho, E. Ruppert Filho, "Automatic characterization system of switched reluctance machines and nonlinear modeling by interpolation using smoothing splines", *IEEE Access*, vol. 6, pp. 26011–26021, 2018, doi:10.1109/ACCESS.2018.2825607.

[16] Z. Lin, D. S. Reay, B. W. Williams, X. He, "Online modeling for switched reluctance motors using B-spline neural networks", *IEEE Transactions on Industrial electronics*, vol. 54, no. 6, pp. 3317–3322, 2007, doi:10.1109/TIE.2007.904009.

[17] C. Li, G. Wang, Y. Li, A. Xu, "An improved finite-state predictive torque control for switched reluctance motor drive", *IET Electric Power Applications*, vol. 12, no. 1, pp. 144–151, 2018, doi:10.1049/iet-epa.2017.0268.

[18] X. Sun, K. Diao, G. Lei, Y. Guo, J. Zhu, "Real-time HIL emulation for a segmented-rotor switched reluctance motor using a new magnetic equivalent circuit", *IEEE Transactions on Power Electronics*, vol. 35, no. 4, pp. 3841–3849, 2019, doi:10.1109/TPEL.2019.2933664.

[19] X. Xue, K. W. E. Cheng, S. L. Ho, "Optimization and evaluation of torque-sharing functions for torque ripple minimization in switched reluctance motor drives", *IEEE transactions on power electronics*, vol. 24, no. 9, pp. 2076–2090, 2009, doi:10.1109/TPEL.2009.2019581.

[20] V. P. Vujičić, "Minimization of torque ripple and copper losses in switched reluctance drive", *IEEE transactions on power electronics*, vol. 27, no. 1, pp. 388–399, 2011, doi:10.1109/TPEL.2011.2158447.

[21] H. Li, B. Bilgin, A. Emadi, "An Improved Torque Sharing Function for Torque Ripple Reduction in Switched Reluctance Machines", *IEEE Transactions on Power Electronics*, vol. 34, no. 2, pp. 1635–1644, 2019, doi:10.1109/TPEL.2018.2835773.

[22] G. Fang, J. Ye, D. Xiao, Z. Xia, X. Wang, A. Emadi, "Time-Efficient Torque Shaping for Switched Reluctance Machines From Linear Space", *IEEE Transactions on Power Electronics*, vol. 36, no. 8, pp. 9361–9371, 2021, doi:10.1109/TPEL.2021.3056287.

[23] Z. Xia, B. Bilgin, S. Nalakath, A. Emadi, "A New Torque Sharing Function Method for Switched Reluctance Machines With Lower Current Tracking Error", *IEEE Transactions on Industrial Electronics*, vol. 68, no. 11, pp. 10612–10622, 2021, doi:10.1109/TIE.2020.3037987.

[24] Z. Xia, G. Fang, D. Xiao, A. Emadi, B. Bilgin, "An Online Torque Sharing Function Method Involving Current Dynamics for Switched Reluctance Motor Drives", *IEEE Transactions on Transportation Electrification*, vol. 9, no. 1, pp. 534–548, 2023, doi:10.1109/TTE.2022.3183171.

[25] M. Bacic, "On hardware-in-the-loop simulation", *in Proceedings of the 44th IEEE Conference on Decision and Control*, pp. 3194–3198, 2005, doi:10.1109/CDC.2005.1582653.

[26] A. Bouscayrol, "Different types of Hardware-In-the-Loop simulation for electric drives", *in 2008 IEEE International Symposium on Industrial Electronics*, pp. 2146–2151, 2008, doi:10.1109/ISIE.2008.4677304.

[27] J. S. Lee, G. Choi, "Modeling and hardware-in-the-loop system realization of electric machine drives—A review", *CES Transactions on Electrical Machines and Systems*, vol. 5, no. 3, pp. 194–201, 2021, doi:10.30941/CESTEMS.2021.00023.

[28] C. Dufour, S. Cense, J. Bélanger, "FPGA-based switched reluctance motor drive and DC-DC converter models for high-bandwidth HIL real-time simulator", *in 2013 15th European Conference on Power Electronics and Applications (EPE)*, pp. 1–8, IEEE, 2013, doi:10.1109/EPE.2013.6632007.

[29] C. Dufour, S. Cense, J. Belanger, "An FPGA HIL Reconfigurable Testing Platform for Vehicular Traction Systems", *in 2014 IEEE Vehicle Power and Propulsion Conference (VPPC)*, pp. 1–4, 2014, doi:10.1109/VPPC.2014.7007012.

[30] F. E. Fleming, C. S. Edrington, "Real-time emulation of switched reluctance machines via magnetic equivalent circuits", *IEEE Transactions on Industrial Electronics*, vol. 63, no. 6, pp. 3366–3376, 2016, doi:10.1109/TIE.2016.2521343.

BIOGRAPHIES

Gustavo Xavier Prestes (Student, IEEE) received the M.Eng. degrees from Technological Institute of Aeronautics in 2011. In 2014, he joined the Federal University of Roraima, where he is currently a professor in electrical engineering department. In 2021 he started a Ph.D degree from the Federal University of Santa Maria, at Santa Maria / RS. His research interests include real-time control applications problems, especially applied to power electronic converters and electric motor drives.

Filipe P. Scalcon (Member, IEEE) received the B.Sc., M.Sc. and Ph.D. degrees in electrical engineering from the Federal University of Santa Maria (UFSM), Santa Maria, RS, Brazil, in 2017, 2019 and 2021, respectively. During that period, he conducted research as a member of the Power Electronics and Control Research Group (GEPOC), UFSM. From January 2022 to January 2024, he was a Postdoctoral Research Fellow with McMaster Automotive Resource Centre (MARC), McMaster University, Hamilton, ON, Canada.

He is currently a Postdoctoral Associate at the University of Calgary, Calgary, AB, Canada. His research interests include electrical machine drives, renewable energy conversion, reluctance machines and digital control.

Babak Nahid-Mobarakeh (Fellow, IEEE) received the Ph.D. degree in electrical engineering from the Institut National Polytechnique de Lorraine, Nancy, France, in 2001. From 2001 to 2006, he was with the Centre de Robotique, Electrotechnique et Automatique, University of Picardie, Amiens, France. In September 2006, he joined the Ecole Nationale Superieured'Electricite et de Mecanique, University of Lorraine, Nancy, where he was a Professor until December 2019. Since January 2020, he has been a Professor with McMaster University, Hamilton, ON, Canada. Dr. Nahid-Mobarakeh has authored or co-authored more than 250 international peer reviewed journal and conference papers as well as several book chapters and patents. His main research interests include nonlinear and robust control design of power converters and drives, fault detection and fault tolerant control of electric systems, and design, control, and stabilization of microgrids. Dr. Nahid-Mobarakeh is the recipient of several IEEE awards. He was the General Chair of the 2020 IEEE Transportation Electrification Conference and Expo. Between 2012 and 2019, he served as the Secretary, Vice Chair, Chair, and Past Chair of the Industrial Automation and Control Committee (IACC) of the IEEE Industry Applications Society (IAS). He was also the IACC Committee Administrator and Technical Committee Paper Review Chair of the IEEE IAS. Currently, he is the Vice Chair of the IEEE Power Electronics Society Technical Committee on Electrified Transportation Systems. He is also a member of the Power Electronics and Motion Control (PEMC) Council.

Rodrigo P. Vieira (Member, IEEE) received the B.S. degree from the Universidade Regional do Noroeste do Estado do Rio Grande do Sul (Unijuí), Ijuí, Brazil, in 2007, and the M.Sc. and Dr.Eng. degrees from the Federal University of Santa Maria (UFSM), Santa Maria, Brazil, in 2008 and 2012, respectively, all in electrical engineering.

From 2010 to 2014, he was with the Federal University of Pampa, Alegrete, Brazil. Since 2014, he has been with UFSM, where he is currently a Professor. His research interests include electrical machine drives, sensorless drives, digital control techniques of static converters, and electric vehicles.